Droplet motion in microfluidic networks: Hydrodynamic interactions and pressure-drop measurements

D. A. Sessoms,[1] M. Belloul,[1] W. Engl,[2] M. Roche,[1] L. Courbin,[1] and P. Panizza[1]
[1]*IPR, UMR CNRS 6251, Campus Beaulieu, Université Rennes 1, 35042 Rennes, France*
[2]*CPMOH, UMR CNRS 5798, Université Bordeaux I, 33400 Talence, France*
(Received 26 March 2009; published 31 July 2009)

We present experimental, numerical, and theoretical studies of droplet flows in hydrodynamic networks. Using both millifluidic and microfluidic devices, we study the partitioning of monodisperse droplets in an asymmetric loop. In both cases, we show that droplet traffic results from the hydrodynamic feedback due to the presence of droplets in the outlet channels. We develop a recently-introduced phenomenological model [W. Engl *et al.*, Phys. Rev. Lett. **95**, 208304 (2005)] and successfully confront its predictions to our experimental results. This approach offers a simple way to measure the excess hydrodynamic resistance of a channel filled with droplets. We discuss the traffic behavior and the variations in the corresponding hydrodynamic resistance length L_d and of the droplet mobility β, as a function of droplet interdistance and confinement for channels having circular or rectangular cross sections.

DOI: 10.1103/PhysRevE.80.016317 PACS number(s): 47.60.Dx, 47.57.−s

I. INTRODUCTION

Microfluidic technology permits the handling of very small volumes of fluids, with a high degree of control and reproducibility [1,2]. Moreover, this technique offers the possibility to form nanoliter droplets of uniform size. The prospects offered by droplet microfluidics are numerous and concern many fields [3,4]. In materials science, for instance, the potential of microfluidic synthesis stems from the continuous production of monodisperse droplets and the ability to manipulate and functionalize each object independently on line [5]. This approach thus offers a unique route to the synthesis of calibrated dispersed materials in sizes typically ranging from ten to a few hundred micrometers, with excellent and uncomparable control over size distribution, shape, and internal structure. Examples of newly fabricated materials include polymer particles with nonspherical shapes [6,7], armored bubbles [8], core shells [9], Janus particles [10], and double emulsions [11,12]. The use of droplets as independent single microreactors also offers large promises for the development of lab-on-a-chip devices used for combinatorial chemistry or high-throughput screening [13,14].

A necessary condition for the successful and reliable achievement of these applications is to generate many monodisperse droplets (i.e., individual reactors) that do not lose their integrity while flowing through the system and to control their traffic in the network. However, the presence of nodes and often loops in the microfluidic network notably affect the complexity of the flow behavior of droplets [15–18]. In a recent paper [19], we studied the behavior of droplets in millimeter-size capillary tubes and investigated their partitioning into two outlet channels at a simple T junction. We observed that a droplet arriving at a junction, if it does not break, usually goes to the outlet characterized by the highest flow rate. Since droplets can increase hydrodynamic resistance of a channel, the presence of droplets downstream in each outlet arm can affect the respective flow rates and, therefore, the partitioning at the junction. This collective hydrodynamic feedback modulated by the increased flow resistance induced by the droplets can alter the probability of partitioning and, thus, governs the traffic in capillary tubes.

Here, we build upon recent investigations to (i) further extend and describe our previously introduced theoretical framework [19] of traffic flows in microfluidic networks, (ii) show how this model can be used to analyze our experimental results and thus to obtain the two key variables necessary to describe droplet flow in a channel, namely, the hydrodynamic resistance length of a droplet and its mobility in a channel, and (iii) discuss the different values found for these parameters when using axisymmetric or rectangular cross-section channels and their variations with the droplet confinement.

Our paper is presented as follows. In the first section, we describe in detail a phenomenological model of droplet transport in a linear channel at low Reynolds and capillary numbers, and we check its validity by performing systematic experiments using an axisymmetric millifluidic device.

The second section of the paper is devoted to the study of the repartition of droplets at an asymmetric microfluidic loop or, equivalently, a simple T junction. We first perform numerical simulations based on our derived model of droplet transport in a linear channel, and we use a simple rule for the choice of direction of a droplet at the inlet junction of the loop. With a result obtained from the simulations, we derive a straightforward analytical expression describing traffic flow in such a configuration. This simple theoretical model is then validated by systematic microfluidic experiments.

II. TRANSPORT OF DROPLETS IN A CONSTANT SECTION TUBE

A. Phenomenological model

Most microfluidic digital applications involve the generation of periodic trains of monodisperse droplets [20–26]. To address the behavior of such flows in complex hydrodynamic networks, a necessary step is first to describe and understand transport flows in a simple channel. We model such flows in

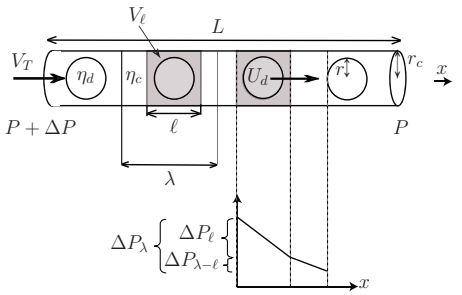

FIG. 1. (Color online) Schematic of the flow model. The pressure drop ΔP occurring across a circular channel of length L and radius r_c results in the flow of the continuous and dispersed phases (viscosities η_c and η_d, respectively). The presence of the dispersed phase in the form of droplets of radius r separated by a distance λ modifies the flow behavior over a length ℓ around each droplet. The speeds of the modified and unmodified flow regions are given by V_ℓ and V_T, respectively, while the droplet speed is U_d. A schematic of the pressure drops in the distinct regions is also shown.

constant cross section S circular conduits at low capillary and Reynolds numbers as follows. First, because of the flow periodicity, we consider the flow only over a channel portion of length λ, corresponding to the droplet interdistance (see Fig. 1). Providing that λ is sufficiently large, so that the droplets do not interact hydrodynamically, we may assume that each droplet modifies the Poiseuille flow only over a small region of length $\ell < \lambda$ (see the shaded area on Fig. 1). We expect ℓ to be, at most, on the order of the size of the channel r_c. Within this simple picture, we decompose the flow in two distinct fluid regions: the region around the droplet and the interdroplet region of length $\lambda - \ell$, where the flow is Poiseuille type.

By assuming for each region that Darcy's laws hold, that is, to say that the velocity of a fluid element is proportional to the pressure drop applied to it, one obtains, for the region altered by the presence of the droplet, the following two equations:

$$V_\ell = K_\ell \frac{\Delta P_\ell}{\ell}, \tag{1}$$

and

$$U_d = K_d \frac{\Delta P_\ell}{\ell}, \tag{2}$$

with U_d and V_ℓ as the velocity of the droplet and the mean velocity of the fluid surrounding it, and with K_d and K_ℓ as two constants that depend on the details of the geometry on Ω, the droplet volume, and on the two viscosities η_d and η_c, respectively. For the other region, one finds a similar relationship for V_T, the continuous phase velocity,

$$V_T = K \frac{\Delta P_{\lambda-\ell}}{\lambda - \ell}. \tag{3}$$

The fluid incompressibility leads to the following relation:

$$Q_T = V_T S = \left(S - \frac{\Omega}{\ell}\right) V_\ell + \frac{\Omega}{\ell} U_d, \tag{4}$$

where Q_T is the total flow rate. By inserting Eqs. (1) and (2) in Eq. (4), a straightforward derivation shows that the droplet velocity varies accordingly to

$$U_d = \beta \frac{Q_T}{S}, \tag{5}$$

where β is a dimensionless coefficient given by

$$\beta = \frac{1}{\frac{K_\ell}{K_d} + \frac{\Omega}{\ell S}\left(1 - \frac{K_\ell}{K_d}\right)}. \tag{6}$$

To obtain an expression for the pressure drop in the channel, we proceed as follows. Since the pressure drop over a tube portion of length λ is the sum of the pressure drops over the two fluid regions,

$$\Delta P_\lambda = \Delta P_\ell + \Delta P_{\lambda-\ell}, \tag{7}$$

a simple calculation yields

$$\Delta P_\lambda = \frac{Q_T}{S}\left[\frac{\lambda}{K} + \ell\left(\frac{\beta}{K_d} - \frac{1}{K}\right)\right]. \tag{8}$$

Then, by considering that the pressure drop for a length L of the channel is simply given by $\Delta P = \frac{L}{\lambda}\Delta P_\lambda$, for the hydrodynamic resistance one obtains a simple relationship of the type,

$$\frac{\Delta P}{Q_T} = \frac{1}{KS}\left[L + \frac{L\ell}{\lambda}\left(\frac{\beta K}{K_d} - 1\right)\right] = \frac{L + nL_d}{KS}, \tag{9}$$

where $n = L/\lambda$ is the number of droplets in the channel and

$$L_d = \ell\left(\frac{\beta K}{K_d} - 1\right) \tag{10}$$

is a constant having dimension of a length. L_d represents the excess length added by each droplet to the channel due to its hydrodynamic resistance. As a simple first approximation, we have neglected the $U_d^{-1/3}$ dependence of the hydrodynamic resistance due to recirculation around the caps of the droplets [27–29] in our model; nevertheless, in the range of capillary numbers used in this work, the dominant contribution to the resistance is the dissipation of the droplets themselves [15]. This observation is also obtained for bubbles flowing in rectangular microfluidic channels for low or high surfactant contents [30].

B. Experiments

Experimentally, we test the validity of our phenomenological model by performing systematic measurements of the droplet velocity and pressure drop of periodic trains of monodisperse droplets flowing through *millifluidic* circular cross-section conduits. To do so, we use an assembly of custom-built modules made of Plexiglas connected to each other by means of calibrated cylindrical glass capillaries or commercial tubing (Fig. 2) [5,19]. The droplet generator is a

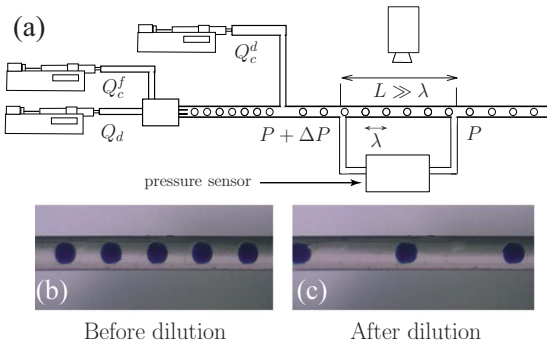

FIG. 2. (Color online) (a) Schematic of the millifluidic setup. Images of the flow (b) at the tip of the needle and (c) after dilution.

double capillary device [31]. It consists of a calibrated syringe needle (diameter 510 μm or 230 μm) centered in a cylindrical capillary tube (radius r_c=750 μm). Using two syringe pumps (Harvard PHD 2000), the dispersed (water) phase and continuous (oil) phase are, respectively, infused through and around the central needle so that droplets form at the tip of the needle with a constant rate of production f. In these millifluidic experiments, the time $\tau=1/f$ separating the formation of two consecutive droplets is typically on the order of 1 s. By fine tuning both Q_d and Q_c^f, the respective flow rates of water and oil, we control Ω, the droplet volume, in the range 0.1–10 μl. An additional infusion of continuous phase performed downstream at constant flow rate Q_c^d increases the distance between two successive droplets λ while keeping their size unchanged. The droplet volume $\Omega=\frac{Q_d}{f}$ and the dilution can thus be controlled independently by changing the values of the various flow rates. We record films of the moving droplets using a video camera (Edmund Optics EO-1312C) at a typical acquisition rate of 50 frames/s, and we use custom-written MATLAB image processing software on these films to determine the droplet velocity U_d and the droplet interdistance λ after dilution. The value of the pressure drop ΔP of a tube portion of length L filled with $n=\frac{L}{\lambda}$ droplets, is obtained with a commercial pressure sensor (ASDX from Sensor Technics, France). We characterize the influence of confinement on droplet flow by systematically varying Ω. For simplicity's sake, we present and discuss our results in what follows in terms of $\rho=\frac{r}{r_c}$, a dimensionless number characterizing the droplet confinement where $r=(\frac{3\Omega}{4\pi})^{1/3}$, assuming the droplets remain nearly spherical throughout the channel. In our experiments, the Reynolds and capillary numbers at play are small (typically on the order of 10^{-2} and 10^{-1}, respectively). We limit our studies to situations where the droplets do not break up at the junction; droplet fragmentation is a phenomenon previously reported for microfluidic channels [32,33] and one that we have also witnessed in our millifluidic experiments at capillary numbers larger than those used here.

In all our experiments [19], we have observed that the droplet velocity varies linearly with the total flow rate ($Q_T=Q_d+Q_c^f+Q_c^d$) accordingly to $U_d=\beta\frac{Q_T}{S}$. The dimensionless coefficient β strongly depends on Ω, the droplet volume (Fig. 3). We have noticed that $1<\beta<2$. For small values of ρ, the variation in β with ρ is well described by the formula

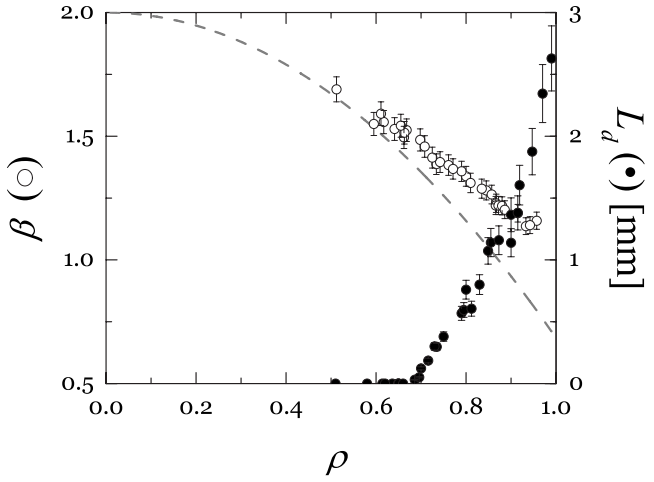

FIG. 3. β (○) and L_d (●) versus ρ. The system is made of water droplets (η_d=1 mPa s) in sunflower oil (η_c=50 mPa s). The dashed line corresponds to the asymptotic model of [34]: $\beta=2-\frac{4\eta\rho^2}{3\eta+2}$ where $\eta=\frac{\eta_c}{\eta_d}$.

analytically derived by Hetsroni *et al.* [34] for an isolated spherical droplet flowing in a cylindrical channel. The droplets in our experiments are therefore sufficiently distant and small so that they do not interact directly with each other and do not rub against the walls with a friction that depends on the capillary number, as in the Bretherton regime [27]. From the measurement of ΔP, we compute the hydrodynamic resistance $\Gamma(L,\Omega,\lambda)=\frac{\Delta P}{Q_T}$ of the portion of tube length L filled with n droplets of volume Ω. For any value of Ω, we note that $\Gamma=\Gamma_o(L)+n\delta_d$ where Γ_o and δ_d are, respectively, the hydrodynamic resistance of the tube with no droplets and the excess hydrodynamic resistance added to the tube by the presence of each droplet (see Fig. 3 in Engl *et al.* [19]). This result is consistent with the prediction [Eq. (9)] of our model. For sake of simplicity, we write $\Gamma(L,\Omega,\lambda)=\Gamma_o(L)(1+\frac{L_d}{\lambda})$. Experimentally, we measure L_d from the slope of $\frac{\Delta P}{Q_T}$ plotted as a function of $\frac{1}{\lambda}$ [19]. The variation in L_d with ρ is reported in Fig. 3. As intuitively expected, we observe that large droplets add more hydrodynamic resistance to the channel than smaller ones. A closer look at our data reveals the existence of two distinct regimes: L_d strongly increases with ρ above a critical value of confinement $\rho_c\simeq 0.7$; whereas its value is essentially zero below ρ_c. To conclude, these simple experiments performed in millifluidic conduits allow a direct measure of both L_d and β, and the results we obtained are well supported by our phenomenological model.

Implementing a standard pressure measurement (using a commercial device) in microfluidic channels remains difficult due to dead volumes and long transient regimes [35–37]. Although several groups have reported clever ways to measure small pressures in microfluidic devices [38–40], to the best of our knowledge, the pressure drop induced by a train of droplets remains ill documented in the literature despite its importance for microfluidics [37]. By contrast, the pressure drops of bubbles along rectangular microchannels are now well documented [30]. In the next section, we will present an indirect measure of L_d, and we will show that the model presented above still holds for microfluidics.

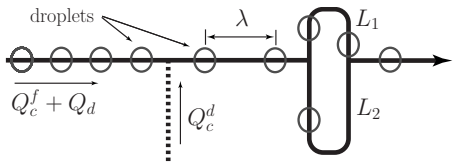

FIG. 4. Schematic representation of the asymmetric loop used in our experiments and simulations.

III. DROPLETS TRAFFIC IN AN ASYMMETRIC LOOP

A. Introduction

To address the general issue of traffic droplet flows in microfluidic networks, we consider the simplest situation where a periodic train of monodisperse droplets flows through an asymmetric loop. We consider a case where the two arms of the loop have different lengths $L_1 < L_2$ but the same cross sections shown schematically in Fig. 4. Similar circuits have been studied in the context of blood flow to understand the phenomenon of *plasma skimming* [41–43], to study the fragmentation of droplets [32,44], the splitting of a stream [45], the dynamics of repartition of droplets at a bifurcation [15], or for the design of a micromixer [46].

This geometry is the microfluidic analog of the millifluidic asymmetric T junction used in our previous work [19] to investigate droplet traffic at a simple junction. However, in contrast to the circular cross section of the millifluidic system, the microfluidic channels present a rectangular cross section. This difference that has important consequences on the flow characteristics will be discussed later in the text.

In this section, we aim to (i) derive the phenomenological model we had briefly introduced in Ref. [19] and discuss the various assumptions made, (ii) show that this model is well suited for understanding and describing traffic flows in microfluidic network, and (iii) demonstrate that the partitioning of droplets at a junction offers an indirect measurement of the hydrodynamic resistance length.

B. Numerical simulations

We first address this problem with a numerical model inspired by the work of Ref. [15]. We will next study how the droplets statistically divide between the two branches of the asymmetric loop, namely, what is the probability P_2 that a droplet bifurcates toward the longest arm? We limit our analysis to the collective hydrodynamic feedback or resistor regime obtained when the droplets are sufficiently large and diluted so that no collisions occur at the inlet junction of the loop [47]. In our analysis of this problem, we assume that the capillary and Reynolds numbers are small enough so that the transport of droplets in the various arms is well accounted by the simple theory developed in the first section of this paper.

We consider a simple system consisting of a single inlet channel through which droplets emitted at a constant frequency $f=\frac{1}{\tau}$, where τ is the (dimensionless) time step in our simulation. In this inlet channel, the droplets travel at constant velocity $U_d=\frac{\lambda}{\tau}$, where λ is the droplet interdistance. The channel splits at a T junction into two arms forming a loop whose respective lengths are $L_2 > L_1$ but whose cross section is the same. Assuming that the droplets do not split at the junction, we numerically investigate their partitioning at the junction. Our simulations are performed as follows. For each time increment τ, a new droplet arrives at the junction. It bifurcates into the outlet having the smallest instantaneous hydrodynamic resistance, and it travels along this arm with a constant velocity $U_d^{(i)}$. Assuming that L_d is the excess length added by each droplet to a channel and neglecting the physical volume of the droplets (a good assumption if the volume fraction is small), the hydrodynamic resistance of the branch (i) is simply given by $R_i(n_i)=\alpha(L_i+n_iL_d)$, where n_i is the number of droplets contained in the branch (i) at the considered time and α a constant (having dimensions of Pa s m^{-4}), function of the viscosity of the continuous phase and of the geometrical parameters defining the channel cross section. For rectangular channels, having width W and height H, at low Reynolds number, it can be shown that $\alpha \simeq 12[1-\frac{192H}{\pi^5 W}\tanh(\frac{\pi W}{2H})]^{-1}\frac{\eta}{WH^3}$, where η is the viscosity of the fluid [48]. Accordingly to the model describing droplet transport in a single channel (see Sec. II), we assume that the velocity of the droplets flowing in the branches obeys $U_d^{(i)}=\beta\frac{Q_T^{(i)}}{S}$, where $Q_T^{(i)}$ is the total flow rate in branch (i). Within this framework, using the conservation of the total flow rate and the equality of the pressure drop between the two branches of the loop, one can show the velocities of the droplets in the two branches are $U_d^{(1)}=U_d\frac{R_2(n_2)}{R_1(n_1)+R_2(n_2)}$ and $U_d^{(2)}=U_d\frac{R_1(n_1)}{R_1(n_1)+R_2(n_2)}$. Using these simple rules, our simulations are performed as follows. Once a new droplet reaches the junction at time t, the hydrodynamic resistances of the two outlets are computed and compared in order to determine the droplet's choice of route through the loop. The velocities of the droplets in each branch of the loop are calculated. The new positions of the droplets as well as the number of droplets present in each branch are then evaluated at time $t+\tau$. If one or several droplets exit the loop between t and $t+\tau$, the number of droplets, their velocities, and their positions in each branch are re-evaluated according to the various times of the exits. Our simulations start with no droplets present in the branches. After an initial transient regime, we observe that the number of droplets n_i present in each branch of the loop fluctuates around their mean values $\langle n_1\rangle$ and $\langle n_2\rangle$ (see Fig. 5). We verified that these stationary values are indeed independent of the initial conditions.

When the train of droplets is diluted, i.e., when λ increases, our numerical simulations show that $\langle n_1\rangle$ and $\langle n_2\rangle$ decrease [see Figs. 5(a)–5(c)]. Above a critical value $\lambda=\lambda_f$, we observe no droplets flowing into the longest branch; $\langle n_2\rangle=0$, as shown in Fig. 5(d). This observation corroborates our previous results, showing the existence of a *filter* regime where the droplets all collect into the smallest branch of the loop and another regime (the *repartition* regime), where they divide between both branches.

Next, we study the variation in $\langle n_1\rangle$ and $\langle n_2\rangle$ with λ shown in Fig. 6. In the repartition regime, we observe that $\langle n_1\rangle-\langle n_2\rangle$ is constant for given values of L_1, L_2, and L_d, as seen in the inset of Fig. 6. A systematic study of this difference as a function of L_d shows that the difference in mean droplet numbers satisfies the following relation $\langle n_1\rangle-\langle n_2\rangle=\frac{L_2-L_1}{L_d}$, as illustrated in Fig. 7. This result indicates that the

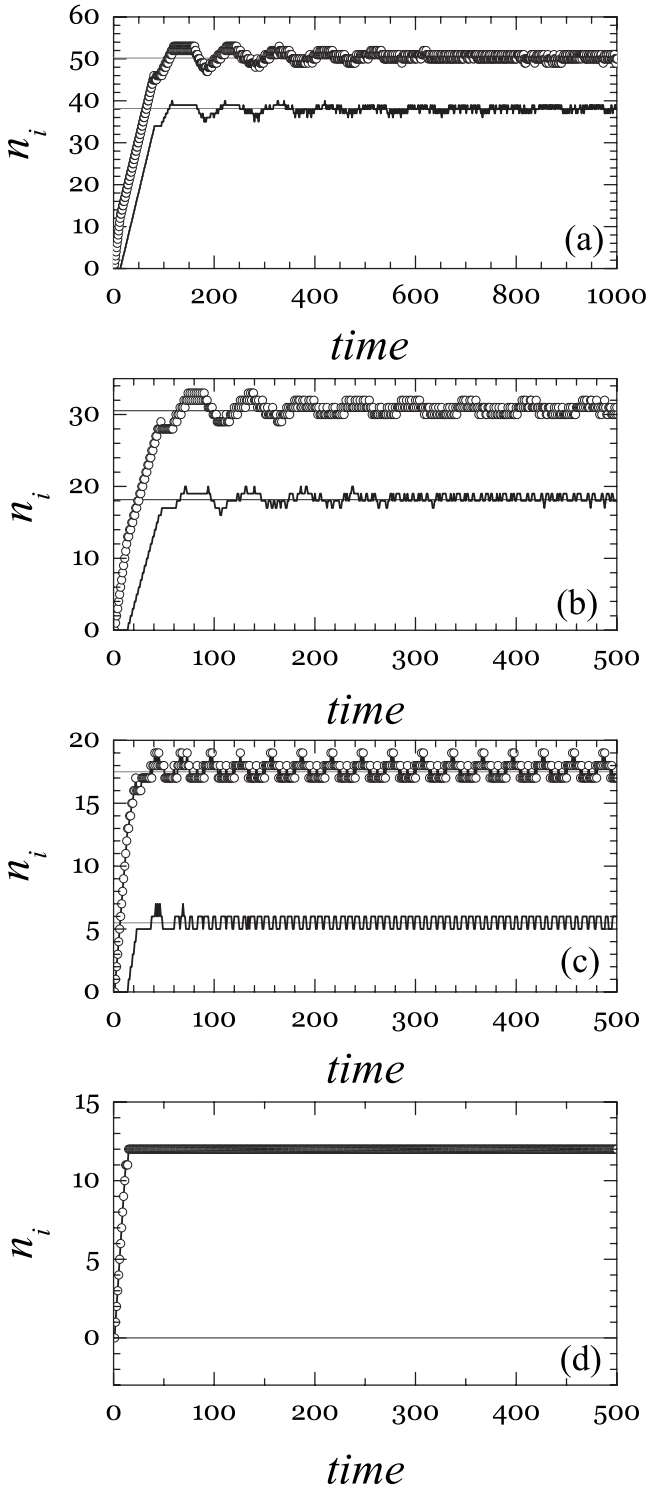

FIG. 5. The variation in n_1 (line and symbols) and n_2 (continuous line) versus time (in τ unit). The time origin corresponds to the entrance of the first droplet in the loop. The parameters (given in the same arbitrary units) are $L_1=100$ and $L_d=2.5$, (a) $\lambda=2$, (b) $\lambda=4.4$, (c) $\lambda=9$, and (d) $\lambda=16$. In these simulations, $\Lambda=1.3$.

hydrodynamic resistances of the two branches of the loop are thus nearly equal once the steady state is reached since $L_1+\langle n_1\rangle L_d \simeq L_2+\langle n_2\rangle L_d$.

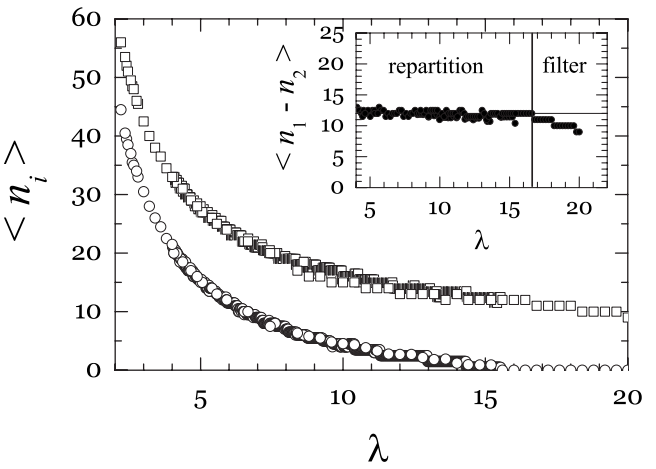

FIG. 6. Shown are $\langle n_1\rangle$ (○) and $\langle n_2\rangle$ (□) versus λ for $L_1=100$, $L_d=2.5$ (given in the same arbitrary unit length), and $\Gamma=1.3$. Inset: shown is $\langle n_1-n_2\rangle$ versus λ.

This result is quite surprising since it implies that the total flow rate in the two branches is equal. Indeed, it is well known for simple fluids, one would expect the total flow rate to be larger in the shortest arm. We can therefore state that $U_d^{(1)}=U_d^{(2)}=\frac{U_d}{2}$. This result can be verified by noting that the mean retention times of the droplets flowing in both branches vary as $\frac{2L_i\tau}{\lambda}$ (see Fig. 8).

In the repartition regime, after reaching the steady state, we compute the probability P_2 that a droplet flows through the longest arm of the loop. We first work for a given value of $\Lambda=\frac{L_2}{L_1}$ and we vary L_d. We have verified that the results obtained for a given Λ do not differ significantly for different values of L_1 provided that the fluctuations of the number of droplets in each arm are small with respect to their mean values. Figure 9 shows the variation in P_2 as a function of λ for different values of L_d. We note that all curves decrease linearly with λ; the curves have different slopes but all share the same intercept. Plotted as a function of $\frac{\lambda}{L_d}$, we notice that all our data collapse on the same straight line (see the inset of Fig. 9).

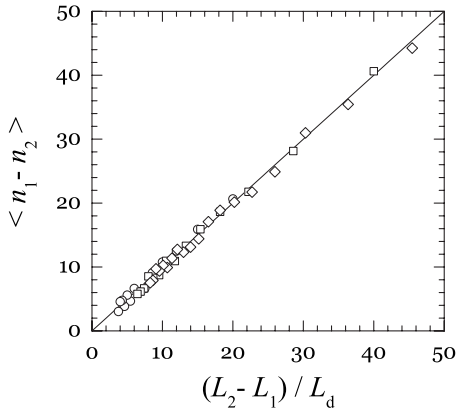

FIG. 7. The mean difference in the number of droplets in the branches as a function of $(L_2-L_1)/L_d$, for $L_1=100$, $L_2=130$ (○); $L_1=100$, $L_2=150$ (□); and $L_1=200$, $L_2=260$ (◇). The lengths are given in terms of the same arbitrary unit length. The line corresponds to the relation $\langle n_1-n_2\rangle=(L_2-L_1)/L_d$.

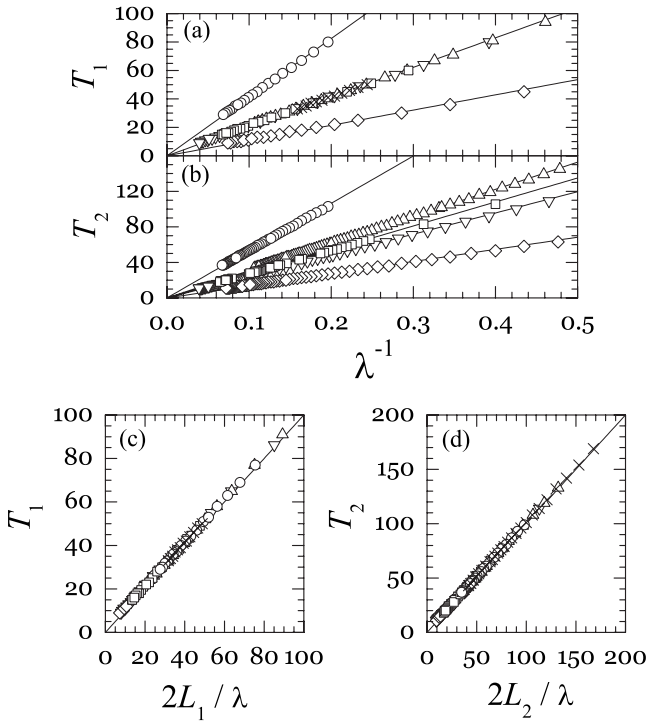

FIG. 8. Residence times for values of (L_1, L_2, L_d), respectively (200,260,2.5) (○), (100,130,2.5) (□), (50,65,2.5) (◇), (100,150,2.5) (△), (100,116,2.5) (▽), and (100,130,1) (×). The lines are best fits through the origin. (a) and (b) Droplet residence times T_1 and T_2 in the shorter and longer branches, respectively, (in τ units) versus λ^{-1}. (c) and (d) Residence times T_i in each arm plotted versus the respective normalized length $\frac{2L_i}{\lambda}$.

In another set of numerical experiments, we impose L_d and study how P_2 changes with λ for different values of L_d. These data reported on Fig. 10 show that all curves decrease linearly with λ. It is worth noting that large values of Λ favor the filter regime over repartition. Moreover, the different intercepts for each curve indicate that the value $P_2(\lambda=0)$ depends solely on the channel length asymmetry ratio Λ and not on L_d.

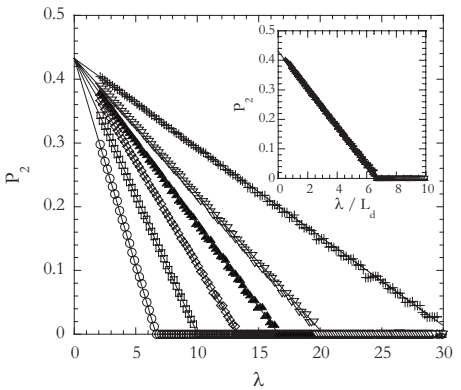

FIG. 9. The probability P_2 of a droplet flowing into the longer branch versus λ for $\Lambda=1.3$ and different values of L_d. The values of L_d are 1(○), 1.5 (□), 2 (◇),2.5 (▲), 3 (▽), and 4.5 (×). The different lengths are expressed in the same arbitrary unit. For each data set, we use $L_1=400$ Inset: shown is P_2 versus $\frac{\lambda}{L_d}$.

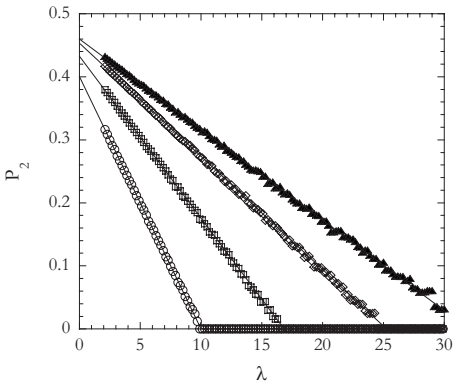

FIG. 10. The probability P_2 versus λ for $L_d=2.5$ and different values of Λ. The values of Λ are 1.5 (○), 1.3 (□), 1.2 (◇), and 1.16 (▲). For each data set, we use $L_1=400$. The different lengths are given in the same arbitrary unit.

In conclusion, our numerical model predicts (i) the existence of two distinct flow states, the filter and repartition regimes; for a given set of Λ and L_d, the transition is determined by a critical value of $\lambda=\lambda_f$, and (ii) that the total flow rates in each branch of the loop are equal in the repartition regime.

C. Analytical model

A rapid analysis of the numerical problem reveals the existence of only four parameters (L_1, L_2, L_d, and λ), all having dimensions of a length. We therefore expect our numerical findings to exhibit universality in terms of at most three dimensionless numbers. We thus now derive analytically expressions for P_2 and λ_f in terms of these dimensionless numbers. Using assumptions identical to those of the numerical model, one may write for each arm of the loop,

$$U_d^{(i)} = \beta \frac{Q_T^{(i)}}{S} = \lambda_i f_i, \tag{11}$$

where $U_d^{(i)}=\lambda_i f_i$, $Q_T^{(i)}$, λ_i, and f_i are, respectively, the droplet velocity and the total flow rate in the arm (i), the mean distance, and the frequency of passage between two successive droplets flowing in arm (i) (with $i=1$ or 2).

The droplet volume is given by

$$\Omega = \frac{Q_d^{(i)}}{f_i} = \frac{Q_d}{f}, \tag{12}$$

with $Q_d^{(i)}$ is the flow rate of dispersed phase in arm (i). Since the hydrodynamic resistance in each arm is given by

$$\frac{\Delta P}{Q_T^{(i)}} = \frac{L_i + n_i L_d}{KS} = \frac{L_i}{KS}\left(1 + \frac{L_d}{\lambda_i}\right), \tag{13}$$

we can write

$$\Lambda\left(1 + \frac{L_d}{\lambda_2}\right) Q_T^{(2)} = \left(1 + \frac{L_d}{\lambda_1}\right) Q_T^{(1)}. \tag{14}$$

From the conservation of the dispersed phase $Q_d=Q_d^{(1)}+Q_d^{(2)}$, one obtains the following relation $f_1+f_2=f$. Inserting

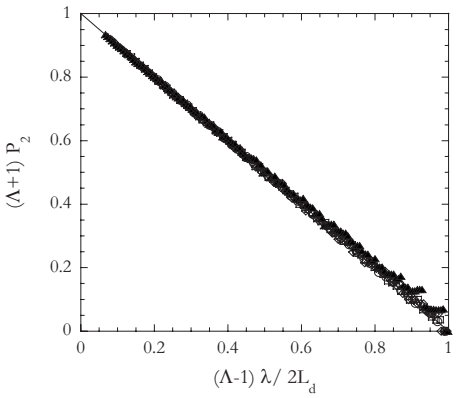

FIG. 11. $(\Lambda+1)P_2$ as a function of $(\Lambda-1)\frac{\lambda}{2L_d}$. The symbols are the same as in Fig. 10. All data collapse onto a single master curve.

this expression in the conservation of the total flow rate, we find

$$\frac{1}{\lambda_1}+\frac{1}{\lambda_2}=\frac{2}{\lambda}. \tag{15}$$

Our numerical results have shown that the total flow rates in each arm are equal. This relation reduces the latter equation to

$$\Lambda\left(1+\frac{L_d}{\lambda_2}\right)=1+\frac{L_d}{\lambda_1}. \tag{16}$$

By solving the system of Eqs. (15) and (16), one obtains the following expressions for λ_2:

$$\frac{1}{\lambda_2}=\frac{1}{\Lambda+1}\left(\frac{2}{\lambda}-\frac{\Lambda-1}{L_d}\right)=\frac{2}{\lambda}-\frac{1}{\lambda_1}. \tag{17}$$

Using this expression and the equality of the flow rates in each arm $U_d^{(2)}=\lambda_2 f_2=\frac{\lambda f}{2}$, we find

$$P_2=\frac{f_2}{f}=\frac{1}{\Lambda+1}\left(1-\lambda\frac{\Lambda-1}{2L_d}\right). \tag{18}$$

To verify this relation, we replot the numerical results presented in Fig. 10 using renormalized axes. As shown in Fig. 11, when we plot $(\Lambda+1)P_2$ as a function of $(\Lambda-1)\frac{\lambda}{2L_d}$, we note that all data collapse onto a single master curve, in agreement with our analytical model and indicating the universal nature of the problem. The probability that a droplet bifurcates toward the longest arm then decreases linearly with λ. Above a critical value λ_f, all droplets are directed toward the smallest arm; this is the filter regime,

$$\lambda_f=\frac{2L_d}{\Lambda-1}. \tag{19}$$

D. Experimental results

We test the validity of our phenomenological model with a series of microfluidic channels whose central feature is an asymmetric loop. The channels are cast using standard polydimetylsiloxane soft lithography methods [49]. Using two

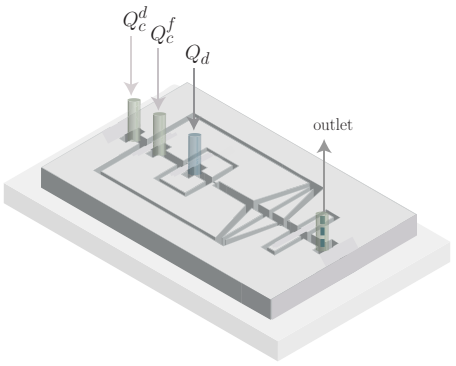

FIG. 12. (Color online) Schematic of the microfluidic chip used to study droplet traffic at a T junction.

syringe pumps (Harvard PHD2000), the droplets are formed in a "flow focusing" geometry [21], where the droplet size can be controlled by changing the respective flow rates Q_c^f and Q_d of the continuous and dispersed phases or by changing the dimensions of the flow constriction. An additional syringe pump is used to add or remove volumes of the continuous phase through supplementary dilution channels to independently control the distance between successive droplets. Similarly to the millifluidic experiments, we denote the flow rate of continuous phase arriving or exiting through the dilution channels as Q_c^d. Finally, the behavior of the droplets at the channel bifurcation is monitored with a high-speed camera (Phantom V7) with a typical acquisition rate on the order of 1000 frames/s. In our microfluidic experiments, the time $\tau=1/f$ separating the formation of two consecutive droplets is typically on the order of 0.02 s. A schematic of our device is shown in Fig. 12. Images of the concentration/dilution module used to change the interdroplet distance λ and the filter and repartition regimes are shown in Fig. 13. We use hexadecane and distilled water as the continuous and disperse phases, respectively, and a small amount of a commercial surfactant (Span 80, 0.3 wt %) is added to the oil phase to hinder droplet coalescence. In these experiments, the Reynolds and capillary numbers are, respectively, on the order of 10^{-2}–10^{-1} and 10^{-2}, roughly the same as those

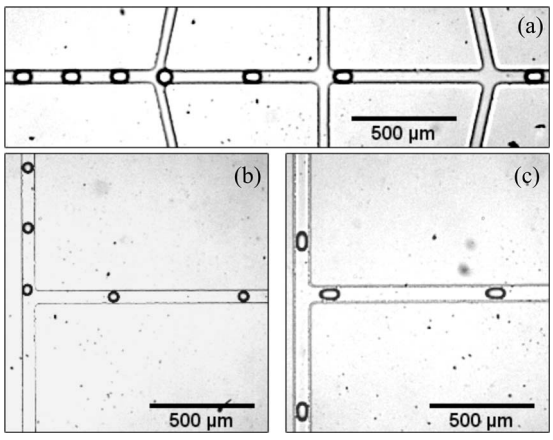

FIG. 13. (a) Images of the concentration/dilution module. Images of the (b) filter regime and the (c) repartition regime observed at the loop inlet.

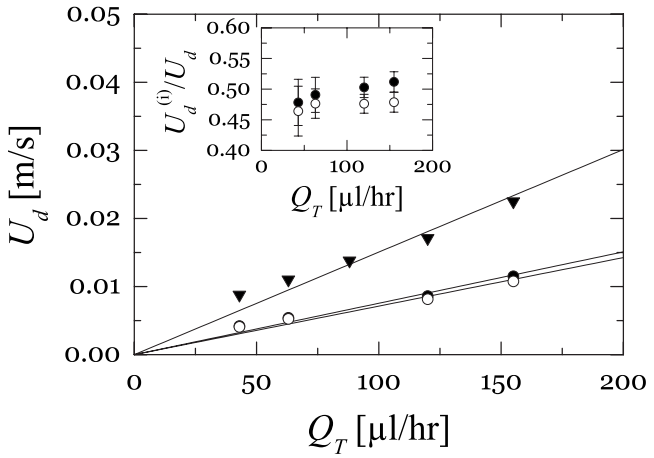

FIG. 14. Droplet speed U_d in the entry channel (▼), short arm (●), and long arm (○) as a function of the total flow rate for $\rho = 1.3$. Each line represents the best linear fit through the origin. Inset: speed in each bifurcation arm $U_d^{(i)}$ normalized by the droplet speed in the entry channel.

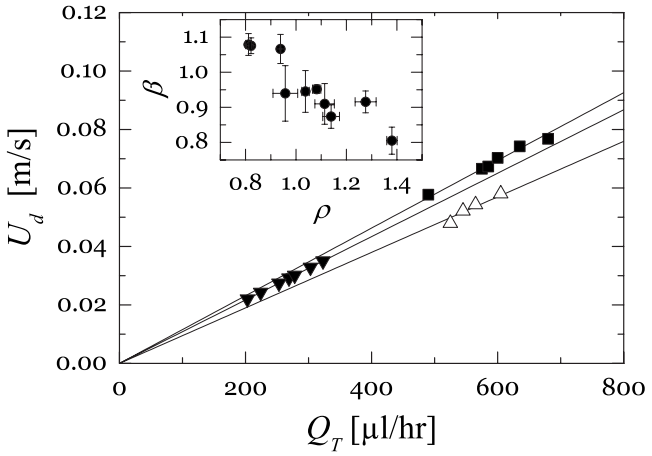

FIG. 15. Droplet speed U_d versus total flow rate Q_T for three different values of the confinement factor ρ; $\rho=0.81$ (■), $\rho=1.08$ (▼), and $\rho=1.11$ (△). Each line represents the best linear fit through the origin. Inset: dimensionless speed factor β as a function of ρ.

found in our millifluidic investigations. Note, however, that the presence of this surfactant implies that the water-oil interface is "solid" in contrast to experiments described in Sec. II for which the interface is "fluid."

We perform experiments on channels with three different length asymmetry ratios $\Lambda=1.1$, 1.2, and 1.3. Nevertheless, all channels have the same cross section, with a width $W=90$ μm and a height $H=29$ μm. The noncircular cross section makes a straightforward determination of the confinement parameter ρ problematic. However, as the channel height is much smaller than its width, the droplets are always strongly confined vertically, with $\Omega \gg H^3$ for all our experiments. Therefore, we are able to focus our investigations onto the effect of lateral confinement within the channel and define $\rho=\frac{2r}{W}$, where r is the radius of the quasicylindrical or "sandwiched" droplet. We find that the droplet speed U_d varies linearly with the total applied flow rate Q_T, as shown for the entry channel and the long and short arms of the bifurcation in Fig. 14. We further note that within the repartition regime, the droplet speeds in the two arms are the same and approximately one-half the entry speed, as seen in the inset of Fig. 14, in agreement with our numerical simulations. Using the relation $U_d=\beta\frac{Q_T}{S}$, we extract the dimensionless speed coefficient β. For deformable droplets in a channel with a circular cross section, $1<\beta<2$ for all droplet sizes. These limits can be understood simply by considering the properties of Poiseuille flow in cylindrical channels. When the droplets are small, they are centered in the channel, where it is well known that the flow speed approaches its maximum, or twice the average flow speed. On the other hand, when the droplet is large and blocks the channel, it moves at the same average velocity as the entire fluid mixture. By contrast, for our droplets in channels with a rectangular cross section, we find that β decreases below 1 for $\rho>1$, as seen in the inset of Fig. 15. This behavior is similar to that observed for gas bubbles in rectangular channels [17], where the value of β can be less than one, depending on the surfactant concentration in the continuous phase. This implies that the continuous phase is able to flow around the edges or "gutters" of the elliptical droplet and points to the importance of corner flows in determining the motion of the dispersed phase.

To compare our experimental results on the partition of droplets at the T junction to our model and our simulations, we measure the probability of a droplet traveling down the long arm of the bifurcation for several droplet sizes. The results for $\Lambda=1.1$, 1.2, and 1.3 are shown in Figs. 16(a)–16(c); indeed, the data show good agreement with a fit to Eq. (18) (solid lines). In this way, passively monitoring the choice of direction of successive droplets at the T junction allows us to measure the hydrodynamic resistance L_d of a single droplet. As a simple test of the consistency of our results, we use the L_d extracted as a fit parameter and renormalize the probability as $(\Lambda+1)P_2$ and the distance as $(\Lambda-1)\frac{\lambda}{2L_d}$ as in the case of the simulations, and we observe a collapse of all data sets onto a single master curve, as seen in Fig. 16(d). We thus confirm the validity of our model over the range of the confinement parameter $0.8\leq\rho\leq1.4$ for these rectangular microchannels.

We estimate the hydrodynamic resistance L_d for all combinations of Λ and ρ and plot the results in Fig. 17. Our experiments show that L_d reaches an asymptotic value of zero when ρ decreases below roughly 0.7 but that the hydrodynamic resistance increases rapidly as the dispersed phase begins to nearly block the channel. Indeed, for $\rho>1$, the presence of even a single droplet adds a significant effective length to the channel, as L_d quickly approaches values of 1 mm, whereas the length of channels in a branching network is typically not much larger than a few tens of millimeters.

IV. CONCLUSION

In conclusion, we have shown that many of the characteristics of immiscible two-phase flows in capillary networks can be captured by a simple analytical model. Our model is derived using straightforward assumptions about the transport of droplets within constant cross-section cylindrical

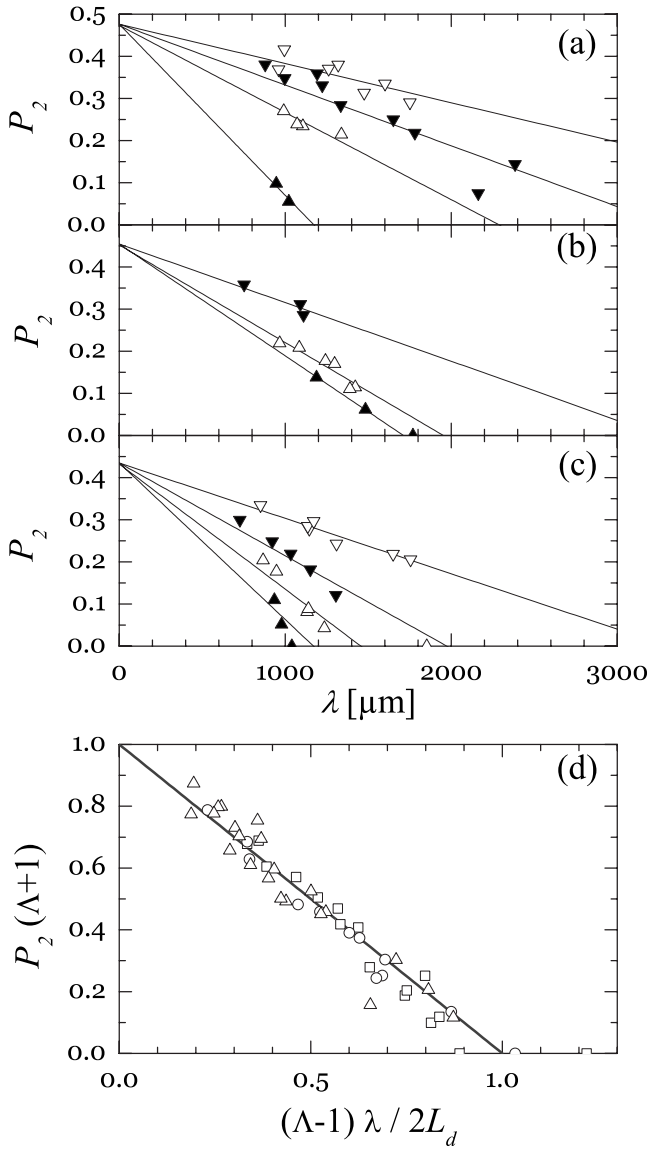

FIG. 16. Probability P_2 versus interdroplet distance for different droplet sizes (symbols) for (a) $\Lambda=1.1$, (b) $\Lambda=1.2$, and (c) $\Lambda=1.3$; the lines are fits to Eq. (18). (d) The renormalized probability for $\Lambda=1.1$ (△), $\Lambda=1.2$ (□), and $\Lambda=1.3$ (○) collapses onto a single master curve.

channels at low Reynolds and capillary numbers. With this approach, flows of droplets are characterized by two phenomenological parameters: the hydrodynamic resistance length L_d added by each droplet to the conduit and the nondimensional droplet mobility coefficient β defined as the ratio of the droplet velocity to the mean flow velocity of the fluids. Systematic experiments performed in millifluidic channels show the validity of this model.

Using this phenomenological approach, we have performed numerical simulations to study the partitioning of droplets at an asymmetric loop. Assuming that a droplet reaching the inlet bifurcation flows into the branch having the smallest instantaneous hydrodynamic resistance, our results show the existence of two hydrodynamic regimes whose transition is governed by λ, the droplet interdistance

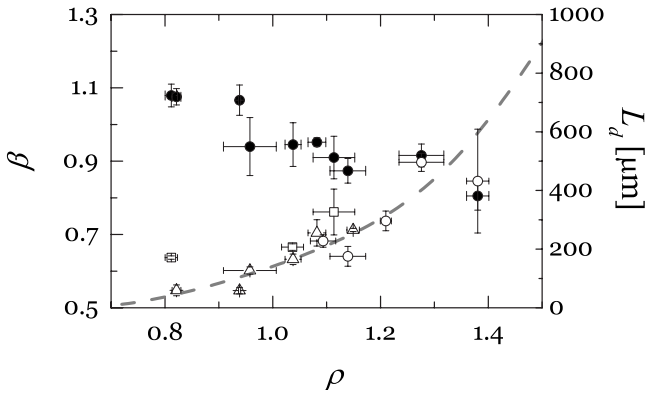

FIG. 17. Dimensionless speed coefficient β (●) and resistance length L_d as a function of confinement ρ [L_d is given for $\Lambda=1.1$ (△), $\Lambda=1.2$ (□), and $\Lambda=1.3$ (○)]. The dotted line is a guide for the eyes.

in the inlet channel. For large values of λ, all droplets flow into the short branch, as its hydrodynamic resistance is always smaller. By contrast, for smaller interdroplet distances, the presence of a large number of droplets in the shorter branch substantially increases the hydrodynamic resistance, leading to the partitioning of droplets between both branches. Our results furthermore show that the probability that a droplet flows into the longest arm exhibits a universal behavior in terms of λ, L_d, and Λ, a nondimensional coefficient characterizing the asymmetry of the loop, a result that can also be derived analytically. Of course, this analysis is valid provided that the droplets are sufficiently distant, i.e., that λ is large enough, where the model of distinct flow regions is correct. In addition, when the drops are close to one another, another mechanism of partitioning comes into play; traffic is then dominated by droplet collisions at the junction [47]. In performing both millifluidic and microfluidic experiments, we have shown the essential validity of our model and simulations. We are able to directly measure the droplet hydrodynamic resistance using a pressure sensor in the millifluidic case or, alternatively, by passively monitoring the probabilities governing the droplet repartitioning in the microfluidic experiments, we are able to extract L_d. In both cases, we observe that L_d increases sharply once the droplets reach a certain critical size. Furthermore, we observe that the rectangular geometry of the microfluidic channels can affect the droplet mobility, as the dispersed phase travels slower than the average flow speed when the droplets are large.

Finding elegant solutions for the passive mixing and sorting of droplets moving through branched microfluidic networks is a great challenge. Understanding the contribution of individual droplets to the global flow behavior of the network is essential to the clever design of such systems [50–52]. We have identified the parameters that are important to tune, i.e., λ and ρ, to modify significantly droplet traffic behavior. Our results emphasize the important role that the droplet size and channel geometry play in determining the flow traffic in capillary networks and should aide the design of more complicated devices, and they pave the way for more systematic studies on the contribution of the fluid viscosity and surfactant concentration to the hydrodynamic resistance.

ACKNOWLEDGMENTS

This work was done with the financial support of an ACOMB grant (ref: Droplets) obtained from the Brittany region of France. D.A.S. gratefully acknowledges support from the Swiss National Science Foundation under Grant No. PB FR-120924. We thank A. Ajdari, N. Bremond, and H. A. Stone for fruitful discussions.

[1] T. Thorsen, S. J. Maerkl, and S. R. Quake, Science **298**, 580 (2002).
[2] H. A. Stone, A. D. Stroock, and A. Ajdari, Annu. Rev. Fluid Mech. **36**, 381 (2004).
[3] M. Joanicot and A. Ajdari, Science **309**, 887 (2005).
[4] A. J. deMello, Nature (London) **442**, 394 (2006).
[5] P. Panizza, W. Engl, C. Hany, and R. Backov, Colloids Surf., A **312**, 24 (2008).
[6] D. Dendukuri, K. Tsoi, T. A. Hatton, and P. S. Doyle, Langmuir **21**, 2113 (2005).
[7] Z. Nie, S. Xu, M. Seo, P. C. Lewis, and E. Kumacheva, J. Am. Chem. Soc. **127**, 8058 (2005).
[8] A. B. Subramaniam, M. Abkarian, and H. A. Stone, Nature Mater. **4**, 553 (2005).
[9] J. W. Kim, A. S. Utada, A. Fernandez-Nieves, Z. Hu, and D. A. Weitz, Angew. Chem., Int. Ed. **46**, 1819 (2007).
[10] Z. Nie, W. Li, M. Seo, S. Xu, and E. Kumacheva, J. Am. Chem. Soc. **128**, 9408 (2006).
[11] S. Okushima, T. Nisisako, T. Torii, and T. Higushi, Langmuir **20**, 9905 (2004).
[12] A. S. Utada, D. R. Link, P. D. Kaplan, H. A. Stone, and D. A. Weitz, Science **308**, 537 (2005).
[13] H. Song and R. F. Ismagilov, J. Am. Chem. Soc. **125**, 14613 (2003).
[14] H. Song, D. L. Chen, and R. F. Ismagilov, Angew. Chem. **45**, 7336 (2006).
[15] F. Jousse, R. Farr, D. R. Link, M. J. Fuerstman, and P. Garstecki, Phys. Rev. E **74**, 036311 (2006).
[16] M. Prakash and N. Gershenfeld, Science **315**, 832 (2007).
[17] M. J. Fuerstman, P. Garstecki, and G. M. Whitesides, Science **315**, 828 (2007).
[18] V. Barbier, H. Willaime, P. Tabeling, and F. Jousse, Phys. Rev. E **74**, 046306 (2006).
[19] W. Engl, M. Roche, A. Colin, P. Panizza, and A. Ajdari, Phys. Rev. Lett. **95**, 208304 (2005).
[20] T. Thorsen, R. W. Roberts, F. H. Arnold, and S. R. Quake, Phys. Rev. Lett. **86**, 4163 (2001).
[21] S. L. Anna, N. Bontoux, and H. A. Stone, Appl. Phys. Lett. **82**, 364 (2003).
[22] P. Garstecki, M. J. Fuerstman, and G. M. Whitesides, Phys. Rev. Lett. **94**, 234502 (2005).
[23] T. Ward, M. Faivre, M. Abkarian, and H. A. Stone, Electrophoresis **26**, 3716 (2005).
[24] P. Garstecki, M. J. Fuerstman, H. A. Stone, and G. M. Whitesides, Lab Chip **6**, 437 (2006).
[25] G. F. Christopher, N. N. Noharuddin, J. A. Taylor, and S. L. Anna, Phys. Rev. E **78**, 036317 (2008).
[26] W. Lee, L. M. Walker, and S. L. Anna, Phys. Fluids **21**, 032103 (2009).
[27] F. P. Bretherton, J. Fluid Mech. **10**, 166 (1961).
[28] H. Wong, C. J. Radke, and S. Morris, J. Fluid Mech. **292**, 95 (1995).
[29] S. R. Hodges, O. E. Jensen, and J. M. Rallison, J. Fluid Mech. **501**, 279 (2004).
[30] M. J. Fuerstman, A. Lai, M. E. Thurlow, S. S. Shevkoplyan, H. A. Stone, and G. M. Whitesides, Lab Chip **7**, 1479 (2007).
[31] C. Cramer, P. Fischer, and E. J. Windhab, Chem. Eng. Sci. **59**, 3045 (2004).
[32] D. R. Link, S. L. Anna, D. A. Weitz, and H. A. Stone, Phys. Rev. Lett. **92**, 054503 (2004).
[33] L. Menetrier-Deremble and P. Tabeling, Phys. Rev. E **74**, 035303(R) (2006).
[34] G. Hetsroni, S. Haber, and E. Wacholder, J. Fluid Mech. **41**, 689 (1970).
[35] K. Hosokawa, K. Hanada, and R. Maeda, J. Micromech. Microeng. **12**, 1 (2002).
[36] M. T. Blom, E. Chmela, F. H. J. van der Heyden, R. E. Oosterbroek, R. Tijssen, M. Elwenspoek, and A. van den Berg, J. Microelectromech. Syst. **14**, 70 (2005).
[37] B. J. Adzima and S. S. Velankar, J. Micromech. Microeng. **16**, 1504 (2006).
[38] A. Groisman, M. Enzelberger, and S. R. Quake, Science **300**, 955 (2003).
[39] M. Abkarian, M. Faivre, and H. A. Stone, Proc. Natl. Acad. Sci. U.S.A. **103**, 538 (2006).
[40] S. A. Vanapalli, D. van den Ende, M. H. G. Duits, and F. Mugele, Appl. Phys. Lett. **90**, 114109 (2007).
[41] R. T. Carr and M. Lacoin, Ann. Biomed. Eng. **28**, 641 (2000).
[42] A. S. Popel and P. C. Johnson, Annu. Rev. Fluid Mech. **37**, 43 (2005).
[43] A. J. Calderon, J. B. Fowlkes, and J. L. Bull, J. Appl. Physiol. **99**, 479 (2005).
[44] M. Yamada, S. Doi, H. Maenaka, M. Yasuda, and M. Seki, J. Colloid Interface Sci. **321**, 401 (2008).
[45] W. Engl, K. Ohata, P. Guillot, A. Colin, and P. Panizza, Phys. Rev. Lett. **96**, 134505 (2006).
[46] P. Garstecki, M. A. Fischbach, and G. M. Whitesides, Appl. Phys. Lett. **86**, 244108 (2005).
[47] M. Belloul, W. Engl, A. Colin, P. Panizza, and A. Ajdari, Phys. Rev. Lett. **102**, 194502 (2009).
[48] C. G. Morris and F. K. Forster, Exp. Fluids **36**, 928 (2004).
[49] D. C. Duffy, J. C. McDonald, O. J. A. Schueller, and G. M. Whitesides, Anal. Chem. **70**, 4974 (1998).
[50] G. Cristobal, J. P. Benoit, M. Joanicot, and A. Ajdari, Appl. Phys. Lett. **89**, 034104 (2006).
[51] L. F. Cheow, L. Yobas, and D. L. Kwong, Appl. Phys. Lett. **90**, 054107 (2007).
[52] X. Niu, S. Gulati, J. B. Edel, and A. J. deMello, Lab Chip **8**, 1837 (2008).